Chapter 10
A Fast and Sensitive Integrated Young Interferometer Biosensor

Johannes S. Kanger, Vinod Subramaniam, Paul H. J. Nederkoorn, and Aurel Ymeti

Abstract We have developed an ultrasensitive biosensor based on an integrated optical Young interferometer. Key features of this sensor are that it is very compact, extremely sensitive, label free, and very fast. Therefore the Young interferometer has significant potential to be developed into a handheld, point-of-care device. In this chapter we review the progress that has been made on the development of integrated Young interferometer sensors. The sensor developed in our lab is discussed in detail. We demonstrate various applications of the current sensor. Special attention is paid to the detection of viruses. Finally a discussion on future prospects of this sensor for diagnostics is given.

10.1   Introduction

The integrated Young interferometer (YI) "immuno sensor" that is discussed in this chapter is one example of a whole class of so-called integrated optical (IO)-based chemical and immuno-sensors. In the past several types of IO sensors have been developed, including waveguide-based sensors such as interferometric sensors[1–6], grating couplers[7], resonant mirrors[8], integrated microcavity-based sensor[9–12], surface plasmon resonance (SPR)-based sensor[13], photonic wire sensors[14], and reflectance-based sensors like reflectance interference device[15].

One of the main advantages of the optical-based sensors is their high resolution. Integrated optical sensors[16], especially the interferometric ones that have been developed in recent years, such as the Mach-Zehnder interferometer (MZI)[17] and the Young interferometer [18–21], show an extremely high refractive index resolution in the range of $10^{-7}-10^{-8}$ RIU (refractive index units) [17,21], which is equivalent to

J.S. Kanger (✉)
Faculty of Science and Technology, University of Twente, Enschede, The Netherlands
e-mail: J.S.Kanger@utwente.nl

detection of a protein mass coverage of ~30 fg/mm^2. Furthermore, the IO readout systems are robust and small, allowing for miniaturization where many elements of the device can be integrated in a single chip occupying a relatively small area. These features offer the prospect for development of multisensing systems. Furthermore, this implies an increase of the analysis throughput, a reduction in the consumption of biomaterials, and cost reduction. Moreover, the optical-based sensors are label free sensing techniques, which require less complex sample preparation, do not need special laboratories and skilled personnel, and result in lower test costs. An additional advantage is that usually a simpler and faster signal analysis can be achieved.

Integrated optical waveguide-based sensors can monitor antibody-antigen interactions by making use of the evanescent field sensitivity of guided modes propagating through the waveguide structure of the sensor. The principle of evanescent field sensing has the advantage that it matches well with the availability of many chemical interfaces. Figure 10.1 shows a scheme of a binding event taking place at the core-cover interface of a three-layer waveguide structure. Here, the core-cover interface of the optical waveguide structure is coated with a chemo-optical transducer receptor layer, which can selectively bind to specific analyte molecules present in the cover medium.

When the binding of an analyte occurs, the substitution of solvent by the analyte molecules will result in an increase of the refractive index n at the core-cover interface. Therefore, the effective refractive index N_{eff} of a guided mode, which probes the core-cover interface during its propagation through the waveguide, will be changed within the interaction length, resulting in a phase change of the mode at the exit of the interaction region.

Here, two different situations can be distinguished: in the first situation, the evanescent region is completely occupied with one material, e.g., a solution of one given analyte (homogeneous sensing) without the benefit of a receptor transduction
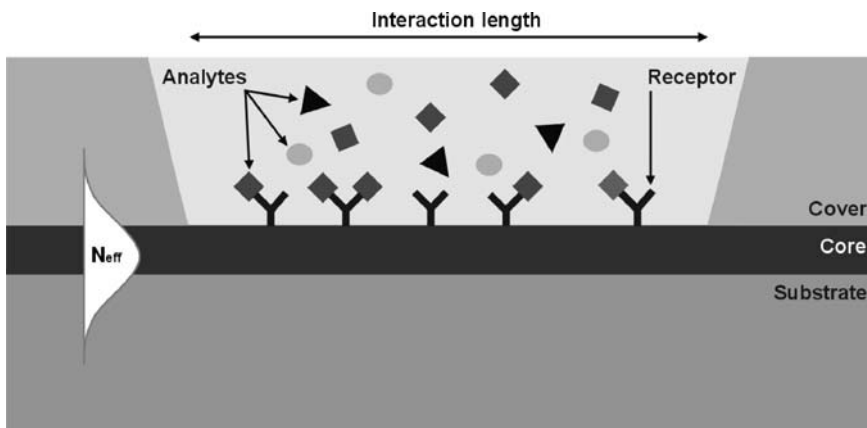

Fig. 10.1 Binding event between analyte and receptor molecules occurring at the core-cover interface of a three-layer waveguide structure within the evanescent region of a guided mode. N_{eff} indicates the effective refractive index of the fundamental guided mode

layer. In this case, the refractive index change is representative of the analyte concentration C in the solution. In the second situation, a chemo-optical transduction layer is immobilized at the core-cover interface of the waveguide structure. For example, in an immunoreaction, this transducer can be an antibody layer (surface sensing).

The phase change that results from a binding event can be measured with a high sensitivity by using an interferometric sensor, e.g., the MZI[17], the YI[19,21], or differential interferometer[22], due to the relatively long interaction lengths of these devices (up to several centimeters). In the group of interferometric devices, those that have a reference branch to compensate for common mode effects, such as temperature changes, pressure changes, fluctuations of light source power, etc., such as the MZI and the YI, are preferable and yield more robust and reproducible results.

Here, we focus on the development of a YI sensor due to its simpler chip design (no optical phase modulation is required to achieve a high sensitivity as in the case of an MZI) and flexibility for development of a multichannel device. In Fig. 10.2, a schematic layout of a two-channel IO YI is shown. Light is coupled into an IO channel waveguide and split by a Y-junction to two parallel output channels positioned at a certain distance from each other, as shown in Fig. 10.2. An interference pattern is generated as a result of the overlap of both outgoing divergent beams. The interference pattern is recorded by a CCD camera, which is placed at a given distance from the endface of the integrated chip. A sensing window is realized on the top of the core layer of the measuring channel where the samples to be analyzed are applied. When a binding event takes place on the sensing window of the measuring channel a phase change between reference and
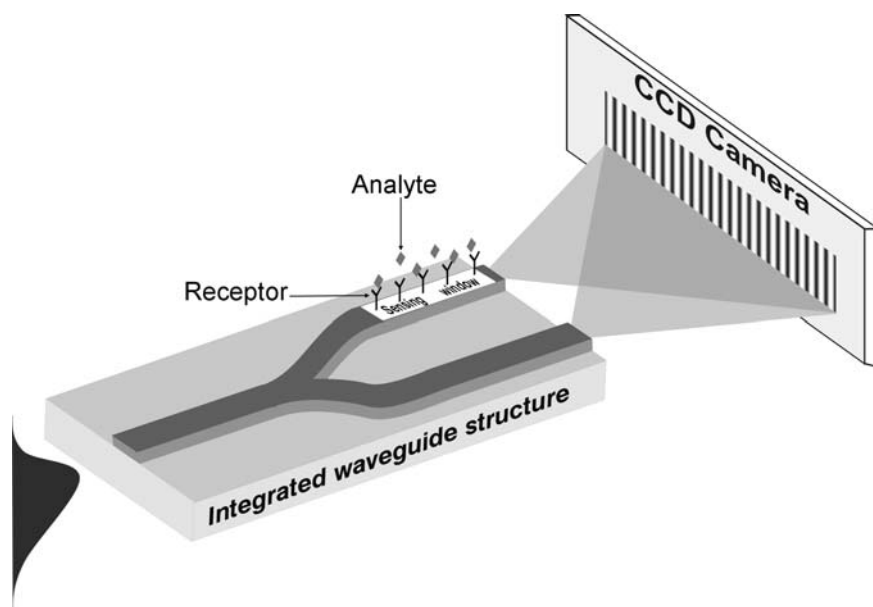

Fig. 10.2 Two-channel integrated optical Young interferometer sensor

measuring channels occurs and the interference pattern will be shifted with respect to the camera surface. By measuring the spatial shift of the interference pattern, the phase change can be calculated, yielding an accurate determination of the refractive index change occurring on the sensing window of the measuring channel.

The interferometric sensors have been mainly used for detection of proteins, e.g., binding of antigen molecules to a specific antibody layer that is immobilized on the sensor surface[19,21,23–26]. It is scientifically interesting and relevant from the application point of view to explore the use of these sensors not only for monitoring proteins, but also for other types of analytes, e.g., viruses, which so far have been detected with time-consuming methods[27]. The principle of the sensor makes possible the detection of relevant viruses such as HIV, SARS, Hepatitis B and C provided that the appropriate specific cognate receptor or antibody is available. Recently the YI sensor has been successfully used to measure low concentrations of HSV-1 virus[28] (see also result section for a detailed description) and Avian Influenza virus[29].

In this chapter we first discuss the fundamentals and the design aspects of an integrated optical YI sensor (Sect. 10.2), followed by a description of the experimental setup (Sect. 10.3). In the result section (Sect. 10.4) both protein and virus detection experiments are discussed. Section 10.5 demonstrates the use of microfluidic chips for efficient sample handling in combination with the YI sensor. This chapter concludes with a discussion on the prospects of the sensor for point-of-care diagnostics.

10.2 Fundamentals

10.2.1 Optical Waveguides

In a three-layer waveguide structure, guiding of the light is performed by engineering appropriate refractive index contrast between the core layer and the cladding. In Fig. 10.1, such a structure is presented, consisting of a substrate, core, and cover layer, which have, respectively, a refractive index of n_S, n_F, and n_C. A higher refractive index of the core layer allows total internal reflection of the light at the core-cladding interface, as shown schematically in Fig. 10.3, making possible propagation of the light through the slab waveguide.

Under conditions of total internal reflection, guided modes are obtained due to the constructive interference between the light rays propagating through the waveguide[30]

$$\frac{2\pi}{\lambda} 2d_F n_F \cos\theta - \Phi_C - \Phi_S = m2\pi, \tag{10.1}$$

where λ is the vacuum wavelength of the guided light, d_F is the thickness of the core layer, θ is the angle of incidence at the core-cladding boundary, Φ_C and Φ_S are the
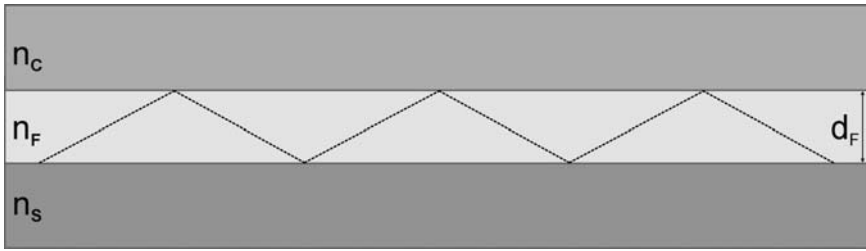
Fig. 10.3 Total internal reflection in a three-layer waveguide structure. n_i ($i = $ C, F, S) indicates the refractive index of layer i of the waveguide structure, $n_F > n_{C,S}$; d_F is the thickness of the core layer
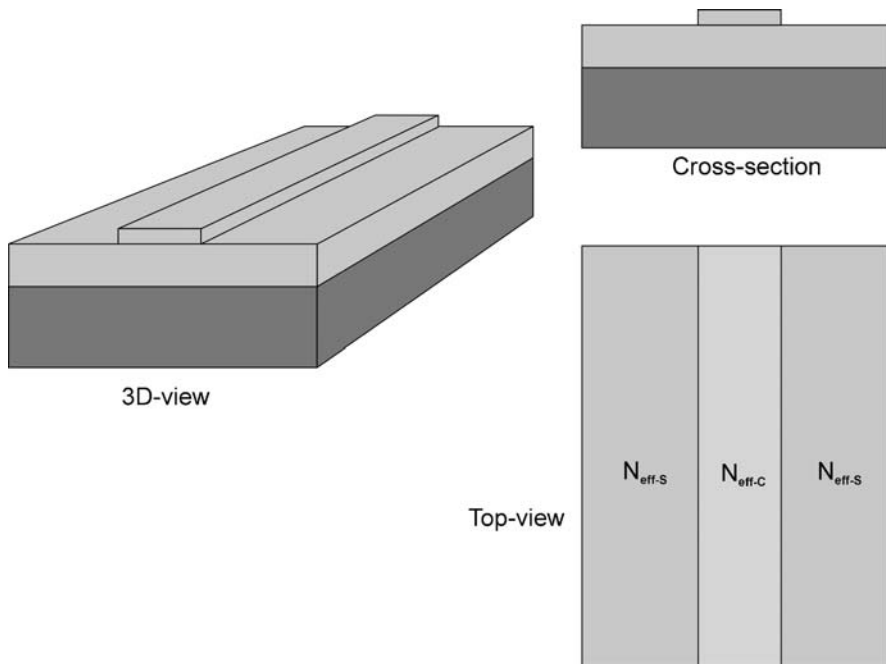

Fig. 10.4 3D-view, cross-section, and *top-view* of a channel waveguide structure; N_{eff-C} and N_{eff-S} indicate the effective refractive indices of the channel and slab region, respectively

phase changes arising from the reflection at the core-cover and core-substrate boundary, respectively, and m is the order of the guided modes.

In a channel waveguide structure, schematically shown in Fig. 10.4, the light is confined not only in the transverse direction, but also in the lateral one. This confinement is caused by the lateral contrast of the (effective) refractive indices between the channel region, N_{eff-C}, and the slab, N_{eff-S}, i.e., $N_{eff-C} > N_{eff-S}$. This contrast can be established by the presence of a ridge in the core section, where the

effective refractive index is defined as $N_{eff} = n_F \sin\theta$. Generally, for a given channel structure the parameters expressing quantitatively the propagation of guided light beams (modes) can be calculated using Maxwell theory-based software.

Finally, channel waveguide structures can be used to guide the light not only along a straight section, but also in a bent one, e.g., in an S-bend, etc.

10.2.2 The YI Sensor

A YI can be designed to have more than two channels. As the two-channel YI sensor is a special case of the more general N-channel or multichannel YI, the theory of the YI is treated for the general N-channel YI. As shown in this section, in the multichannel YI all pairs of parallel output channels act as a two-channel YI, each with a unique distance between its two arms. In Fig. 10.5 the layout of the 4-channel YI sensor described in this chapter is shown.

In a multichannel YI, monochromatic laser light with a vacuum wavelength λ is coupled into an input channel waveguide and split to N output parallel channels, as shown in Fig. 10.5 (in this figure a network of three Y-junctions is used to split the light to four output channels).

The output divergent beams overlap with each other and the final interference pattern is a superposition of individual interference patterns, each of them representing the overlap of the divergent beams of a specific channel pair. The interference pattern is recorded by a CCD camera, which is placed at a distance L from the chip endface. The irradiance distribution of the sum interference pattern at the input face of the camera can be derived to be[32]
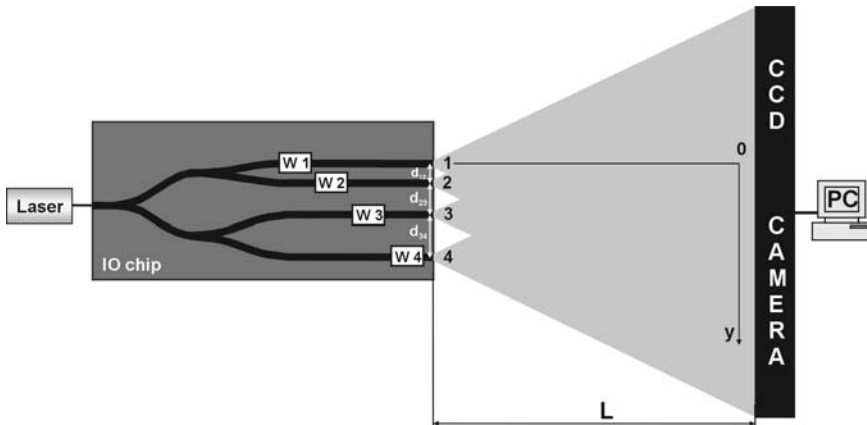

Fig. 10.5 Layout of the four-channel IO YI (not to scale); W_i indicates the sensing window on channel i, d_{ij} is the distance between channels i and j, L indicates the distance of the CCD camera from the chip end-face. Reprinted from Ref. 31 with permission. © 2008 Optical Society of America

$$I(y) \approx \sum_{i=1}^{N} I_i + 2 \sum_{i,j=1; i<j}^{N} (I_i I_j)^{\frac{1}{2}} \cos(\Delta\Phi_{ij}(y) - \Delta\phi_{ij}), \qquad (10.2)$$

where I_i and I_j are the output powers from channels i and j, respectively. A channel output is approximated as a point source. Equation (10.2) is only valid if L is chosen such that the output divergent beams fully overlap at the CCD camera. In (10.2), $\Delta\Phi_{ij}(y)$ is the phase difference between the interfering beams coupled out from channels i and j as a result of their different optical path lengths at the interfering position y on the CCD camera. The phase change $\Delta\phi_{ij}$ represents the sum of the initial phase difference at the channel outputs in absence of the analyte, $\Delta\phi_{ij}{}^0$, and the phase change $\Delta\varphi_{ij} = \Delta\varphi_i - \Delta\varphi_j$ induced by refractive index changes Δn_i and Δn_j in channels i and j, respectively, i.e., $\Delta\phi_{ij} = \Delta\phi_{ij}{}^0 + \Delta\varphi_{ij}$. The phase difference $\Delta\Phi_{ij}(y)$ is given by[32]

$$\Delta\Phi_{ij}(y) = \frac{2\pi}{\lambda}\frac{d_{ij}}{L}y - \frac{2\pi}{\lambda}\frac{d_{ij}}{L}\left(d_{1i} + \frac{1}{2}d_{ij}\right) \qquad (10.3)$$

provided that the distance between channels i and j $d_{ij} << L$ for all i, j values, a condition that is well satisfied in most cases. Hence, an individual interference pattern shows a spatial frequency k_{ij} given as

$$k_{ij} = \frac{1}{\lambda}\frac{d_{ij}}{L}. \qquad (10.4)$$

The second term in (10.3) corrects for the shift of the center between two channels i and j with respect to the origin of the y-axis along the CCD camera (see Fig. 10.5).

The refractive index changes in channels i and j can be induced by binding between analyte and receptor molecules in the sensing window of each channel, or alternatively by a change of analyte concentration in the bulk solution. For both cases the refractive index in (part of) the sensing area of channel i and channel j that is probed by the evanescent field of the guided mode will be affected. As a result, the effective refractive index of guided modes in channels i and j ($N_{\text{eff},i}$ and $N_{\text{eff},j}$ respectively) will be changed, and consequently the phase changes $\Delta\varphi_i$ and $\Delta\varphi_j$ will result. The phase change $\Delta\varphi_{ij} = \Delta\varphi_i - \Delta\varphi_j$ can then be derived as:

$$\Delta\varphi_{ij} = \frac{2\pi}{\lambda}l(\Delta N_{\text{eff},i} - \Delta N_{\text{eff},j}) = \frac{2\pi}{\lambda}l\,\Delta N_{\text{eff},ij}, \qquad (10.5)$$

where l is the length of the sensing window realized on top of each output channel and $\Delta N_{\text{eff},ij} = \Delta N_{\text{eff},i} - \Delta N_{\text{eff},j}$. The resulting refractive index change between channels i and j can cause a spatial shift of Δy_{ij} of the individual interference pattern for this channel pair along the camera surface. This shift can be calculated based on (10.3) and (10.5) as

$$\Delta y_{ij} = \frac{lL}{d_{ij}}\Delta N_{\text{eff},ij.} \qquad (10.6)$$

If one chooses channel i, $i = 1, 2,\ldots, N - 1$, to be the measuring channels, and channel N as a reference channel, where N is the total number of the channels, the refractive index changes $\Delta N_{\text{eff},iN}$ may be determined using (10.6) by measuring the spatial shifts Δy_{iN}. Section 10.2.3 demonstrates that this approach allows determining either the amount of adsorbed analytes on the sensor surface, or alternatively the change in concentration of analytes in the bulk solution.

If $N = 2$, there will be one measuring channel, and this is the case of a two-channel YI device[34]. In case of $N = 4$, the refractive index changes $\Delta N_{\text{eff},14}$, $\Delta N_{\text{eff},24}$, and $\Delta N_{\text{eff},34}$ can be calculated based on the measurement of the spatial shifts Δy_{14}, Δy_{24}, and Δy_{34}.[31] An essential condition is that these spatial shifts have to be measured simultaneously and independently of each other, requiring a proper configuration of the four-channel YI device, which is described next.

The output parallel channels of the multichannel device are positioned at different distances d_{ij} from each other in such a way that channels of each pair are separated by a unique distance, as shown in Fig. 10.5. In other words, $d_{12} \neq d_{23} \neq \ldots \neq d_{ij}$. In this way all spatial frequencies k_{ij}, each of them corresponding to the specific distance d_{ij} as shown from relation (2.4), are different, which makes it possible to well-separate different peaks in the amplitude spectrum of the Fourier-transformed interference pattern and select the spatial frequency for each peak. As a result, the phase change $\Delta\phi_{ij}$ between both channels of one pair, corresponding to the selected spatial frequency k_{ij}, can be monitored independently of the other channel pairs in the phase spectrum of the Fourier-transformed interference pattern.

A more detailed description of the working principle of the multichannel YI is given for a four-channel device ($N = 4$). The distances between the channels have been chosen such that $d_{12} \neq d_{23} \neq d_{34} \neq d_{13} \neq d_{24} \neq d_{14}$. There are six possible different channel pairs corresponding to six different distances of $d_{12} = 60$ μm, $d_{23} = 80$ μm, $d_{34} = 100$ μm, $d_{13} = 140$ μm, $d_{24} = 180$ μm, and $d_{14} = 240$ μm. These distances match the realized YI sensor structure described in Sect. 10.3. The final interference pattern will thus be a superposition of six two-channel interference patterns. The calculated interference pattern for the four-channel YI is shown in Fig. 10.6a. The amplitude spectrum (lower graph) and the phase spectrum (upper graph) of the Fourier-transformed interference pattern are presented in Fig. 10.6b.

As one might expect, there are six different peaks in the amplitude spectrum of the Fourier-transformed interference pattern located at six different spatial frequencies k_{ij}, each of them corresponding to the interference pattern obtained as a result of overlap of the channels that are separated by the specific distance d_{ij}. Looking at the selected spatial frequencies at the phase spectrum of the Fourier-transformed interference pattern, the phase of each "two-channel sensor" can be monitored simultaneously and independently from each other. The difference between distances d_{ij} should be designed such that they allow a good separation of the six different peaks.

If an extra phase change occur in one of the channels, e.g., in channel 1 as a result of the binding of an analyte, the same phase change is expected between channels of those pairs that involve channel 1. In Fig. 10.6a, the dotted line represents the calculated interference pattern when an extra phase change is
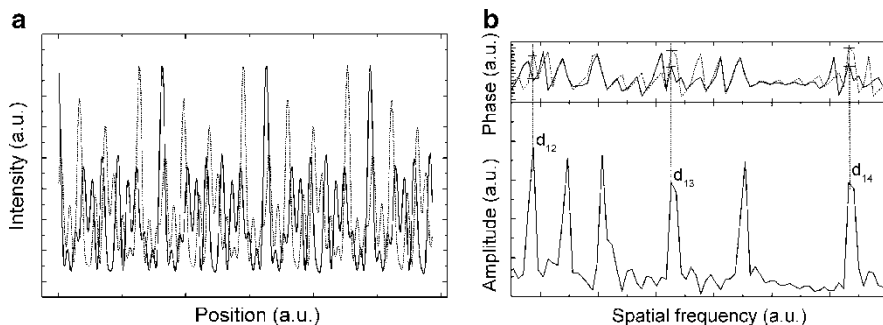
Fig. 10.6 (**a**) The interference pattern in the four-channel YI calculated for $L = 6$ cm, $d_{12} = 60$ μm, $d_{23} = 80$ μm, $d_{34} = 100$ μm (*solid line*). The *dotted line* represents the interference pattern calculated when an extra phase change is introduced on channel 1. (**b**) Amplitude spectrum (lower graph) and the phase spectrum (upper graph) of the Fourier-transformed interference patterns shown in (**a**) (*solid* and *dotted line*, respectively). Reprinted from Ref. 34 with permission. © 2008 Elsevier

introduced in channel 1. Calculation of the Fast Fourier Transform (FFT) of this interference pattern results in six different peaks in the amplitude spectrum of the Fourier-transformed interference pattern, located at the same spatial frequencies when no extra phase change is introduced in one of the channels. In the phase spectrum of the Fourier Transform, one can clearly observe a phase change corresponding to those channel pairs where channel 1 is involved (see dotted line in Fig. 10.6b).

If channels 1, 2, and 3 are chosen as measuring channels and channel 4 as a reference channel, it will be possible in principle to monitor independently and simultaneously three different binding events, each of them taking place in one of the measuring channels.

10.2.3 Analysis of Sensitivity

The sensitivity of the YI describes how the signal (shift of the interference pattern) changes in response to a change of concentration ΔC of the analyte (either adsorbed to the surface of the sensing area or in the bulk solution). Here, the sensitivity chain $\Delta C \Rightarrow \Delta N_{\text{eff}} \Rightarrow \Delta \varphi \Rightarrow \Delta$ (interference pattern) is discussed in detail.

Two different modes of operation are distinguished. The first mode is the detection of changes in bulk concentrations. In this case a change in analyte concentration causes a change of the refractive index of the bulk solution. For the relation between the refractive index change Δn_i and the change in concentration ΔC_i we have:

$$\Delta n_i = \frac{\partial n}{\partial C} \Delta C_i. \tag{10.7}$$

The value of $\partial n/\partial C$ depends on the properties of the material, e.g., in case of proteins this coefficient is ~ 0.188 ml/g[35] and in case of glucose dissolved in water (used for calibration measurements as discussed later in this chapter) this coefficient is ~ 0.069 ml/g[36]. In the second mode of operation, analytes bind to the sensor surface (e.g., mediated by a receptor layer). In this case a thin layer with thickness w and refractive index n_w is formed by the adsorbed analytes. Because the value of n_w (e.g., 1.45 for proteins) is usually different than the refractive index of the solution (e.g., 1.33 for water) that contains the analyte molecules, a phase change is induced. The average layer growth (Δw) on the sensor surface can be related to the mass change (Δm) per surface area (A):

$$\Delta w_i = \rho_w^{-1} \frac{\Delta m_i}{A}, \tag{10.8}$$

where ρ_w denotes the mass density of the adsorbed molecules. Here it is assumed that all channels are identical i.e., $A_i = A$ for all channels i. A value of $\rho_w = 0.6$ mg/mm^3 is estimated for proteins[35]. The changes in either refractive index or adsorbed layer thickness affect the effective refractive index of the guided mode:

$$\Delta N_{\text{eff},i} = \frac{\partial N_{\text{eff}}}{\partial n} \Delta n_i, \tag{10.9a}$$

$$\Delta N_{\text{eff},i} = \frac{\partial N_{\text{eff}}}{\partial w} \Delta w_i. \tag{10.9b}$$

$\partial N_{\text{eff}}/\partial n$ is the sensitivity coefficient of N_{eff} with respect to the change of the refractive index of the bulk, whereas $\partial N_{\text{eff}}/\partial w$ is the sensitivity coefficient of N_{eff} with respect to the change of the adsorbed layer thickness. Again it is assumed that all channels are identical, i.e., $\partial N_{\text{eff},i}/\partial n_i = \partial N_{\text{eff}}/\partial n$ and $\partial N_{\text{eff},i}/\partial w_i = \partial N_{\text{eff}}/\partial w$ for all values of i. In order to have a high sensitivity, $\partial N_{\text{eff}}/\partial n$ and $\partial N_{\text{eff}}/\partial w$ should be maximized. These sensitivity coefficients depends on the refractive indices of the substrate, core, and analyte solution (n_S, n_F, and n_{sol}, respectively), the thickness of the core layer, d_F, the wavelength of the light source, λ, and polarization used either Transverse Electric (TE) or Transverse Magnetic (TM).

Using the SiO$_x$N$_y$ technology, highest sensitivity is obtained[37] by using Si$_3$N$_4$ as material for the core layer of the structure, having the highest refractive index of the SiON family, in combination with the choice of SiO$_2$, a low refractive index material, for the substrate and cover layers.

In addition, $\partial N_{\text{eff}}/\partial n$ and $\partial N_{\text{eff}}/\partial w$ depend on the thickness of the core layer, which at the same time should be chosen such that given the wavelength and polarization, the channel waveguide should be monomode (interference of one mode only is required) in the transverse direction. The width and ridge height of the ridge type channel waveguide should be chosen such that the channel is additionally monomode in the lateral direction, and in such a way that modal field should be maximally confined in the lateral direction. The lateral field profile is preferred to be as small as possible, because this gives the best agreement with the point source approximation used to describe the sensing system (see Sect. 10.2.3).

For the waveguide design as described in Sect. 10.3, the calculated values for both sensitivities are $\partial N_{\text{eff}}/\partial n = 0.21$; and $\partial N_{\text{eff}}/\partial w = 3.1 \times 10^5 \text{ m}^{-1}$ (for $n_w = 1.45$).

The change in N_{eff} causes a change in the phase $\Delta\varphi_{ij}$ of the guided light at the end of the sensing window. Using (10.5) and (10.7–10.9) allows deriving the complete sensitivity chain as (where the subscript "*bulk*" and "*layer*" are used to distinguish between both modes of operation):

$$\Delta\varphi_{ij}^{\text{bulk}} = \frac{2\pi}{\lambda} l \frac{\partial N_{\text{eff}}}{\partial n} \frac{\partial n}{\partial C} \Delta C_{ij}, \tag{10.10a}$$

$$\Delta\varphi_{ij}^{\text{layer}} = \frac{2\pi}{\lambda} l \frac{\partial N_{\text{eff}}}{\partial w} \rho_w^{-1} \frac{\Delta m_{ij}}{A}. \tag{10.10b}$$

Increasing the interaction length, l, or choosing a smaller wavelength λ results in a higher sensitivity of $\Delta\varphi_{ij}$ with respect to N_{eff}. However, l is limited by the size of the chip and for choosing λ, other factors such as scattering losses, which increase when λ decreases, should be considered.

In a final stage, the change of the phase difference causes a change of the interference pattern from which, using Fourier analysis, the $\Delta\varphi_{ij}$ can be derived. This has been treated in Sect. 10.2.2 and has consequences for the distance between the output channels only.

To give an example both sensitivity coefficients are evaluated for the current sensor (see Sect. 10.3 for details). For the bulk detection of glucose this results in $\Delta\varphi^{\text{bulk}}$ (rad) $= 5.6 \times 10^2 \Delta C$ (g/ml), whereas for the adsorption of proteins on the sensor surface the overall sensitivity of the sensor is evaluated as $\Delta\varphi^{\text{layer}}$ (rad) $= 2.0 \times 10^{-5} \Delta m/A$ (fg/mm^2). Measuring the phase change $\Delta\varphi_{ij}$ between any of the two channels i and j can thus give an estimation on the change in analyte concentrations between those two channels. If one channel (e.g., channel N) is used as a reference channel, then $\Delta C_N = 0$ and $\Delta m_N = 0$ and absolute analyte concentrations can be determined.

10.3   Fabrication and Characterization

10.3.1   The Sensor Chip

Based on the analysis presented in the previous section, here the design of the four-channel YI sensor is discussed.

In the four-channel YI sensor single mode channel waveguides are used to split the incoupled light into four parallel channels using a network of three Y-junctions. The single mode character is important as different modes are affected differently by refractive index changes due to, e.g., analyte concentration changes. This will strongly complicate the signal analysis. Coupling of the light to the channel

waveguide is achieved by very efficient fiber-to-chip coupling[17], which results in a robust device. Alternative coupling schemes such as end-fire coupling[38] or grating coupling[39] may also be applied. For optimal fiber-to-chip coupling adiabatic transition from the channel waveguide end-face cross-section to the cross-section of the common waveguide requires transverse adiabatic tapers, which have a small taper angle ($<$0.030) to have functional tapering losses $<$0.1 dB[40]. The distances between the four channels are chosen such that all six possible distances between a set of two channels are distinct in order to allow independent measurements of phase differences (see discussion in Sect. 10.2.2). Furthermore, the distances are chosen such that (a) a reasonable number ($>$2) of fringes are visible at the CCD interface (the channels should not be too close) and (b) there is a good overlap of the light from the different channels at the surface of the CCD (the channels should not be too far apart). Although the distances are not device-critical, it is important to take these considerations into account for an optimal device design.

The final structure design of the four-channel YI sensor is shown in Fig. 10.7: top-view (a), cross-section perpendicular to output channels (b), and side-view along the optical path (c). The distance between the mutually parallel output branches of the first Y-junction is chosen as $D = 160$ μm and the length of the splitting section is $L_{split} \sim 10$ mm.

Besides the limited size of the wafer (4 in.) and the required minimum length of other subfunctions in the optical chip, the need for integrating the four sensing windows with a microfluidic system or a flow-through cuvette further reduces the interaction length. In addition, an interdistance between sensing windows along the channel direction is needed to allow a good alignment of the flow-through cuvette. The length of the four sensing windows is chosen to be $l = 4$ mm (width $w_{win} = 100$ μm) with an interdistance $l_{int} = 3$ mm.

The last two restrictions can be overcome by using a microfluidic system where the sensing windows can be implemented parallel to each other and no interdistance is necessary. In that case, each sensing window can be as long as $\sim$28 mm, resulting in an improvement of the sensitivity by almost 1 order of magnitude.

Table 10.1 summarizes the parameters of the final four-channel YI structure. The IO chips are fabricated using Silicon-oxynitride (cleanroom) technology. Details of the fabrication process have been described extensively elsewhere[41].

10.3.2 Applying the Analytes

Application of sample solutions to the sensing windows of the four-channel sensor is achieved by integrating either a flow-through cuvette or a microfluidic system[42]. These systems are required to simultaneously apply different sample solutions to all four sensing windows. The flow-through cuvette is fixed onto the optical chip by slightly pressing it on the top, whereas the microfluidic system can be permanently bonded to the optical chip.
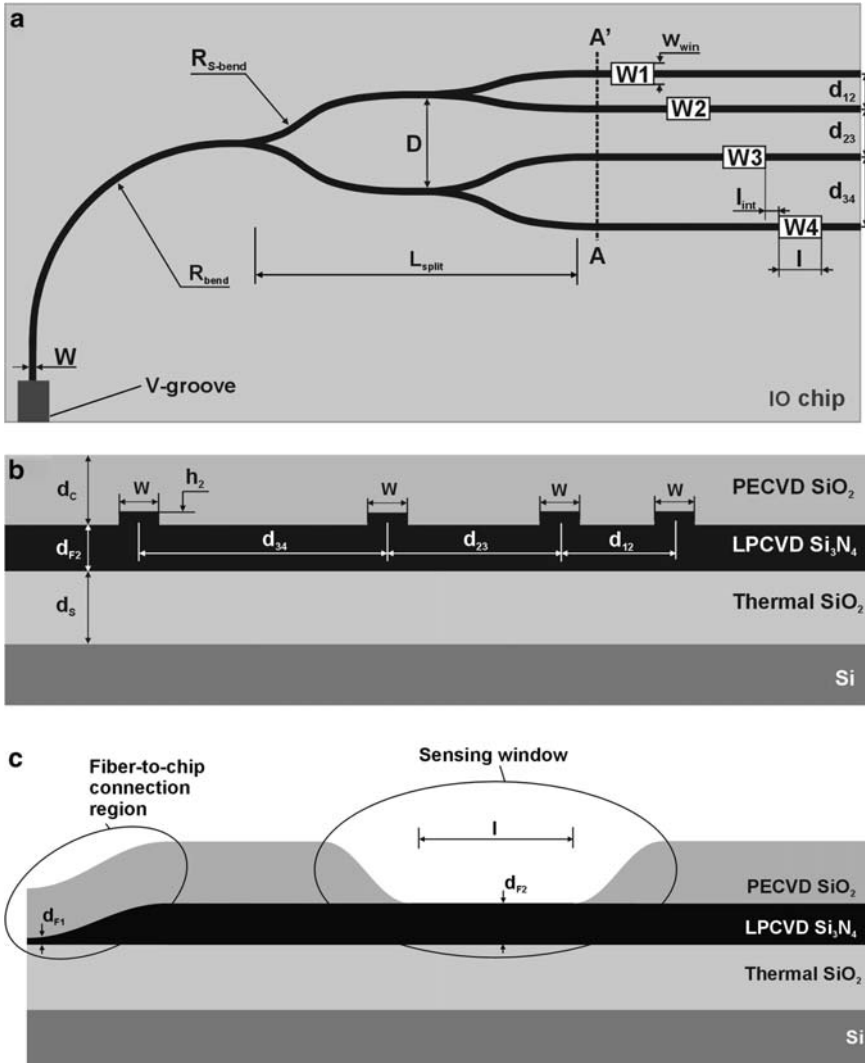
Fig. 10.7 *Top-view* (**a**), cross-section along AA' (**b**), and *side-view* (**c**) of the four-channel IO YI sensor; W_i indicates the sensing window on channel i, d_{ij} indicates the distance between channels i and j, R_{bend} and $R_{S\text{-bend}}$ are the radius of 90°-bend and S-bends, respectively, W is the width of the channel waveguide. The dimensions of the chip are 63 mm × 24 mm

The flow-through cuvette that is used for the four-channel sensor is made from Perspex and is 31-mm long and 7-mm wide. It has four flow chambers each with a volume of 1.2 μl (6 mm long and 3 mm wide), see Fig. 10.8. Each chamber of the cuvette has an inlet and outlet that are connected via a tubing system with the sampling reservoirs, which contain solutions to be monitored, and to the waste, respectively. Samples are flowed by means of a peristaltic pump (Ismatec

Table 10.1 Parameters of the four-channel IO YI sensor

Parameter	Symbol	Value	Dimension
Wavelength of used light	λ	647	nm
Waveguide mode	–	TE_{00}	–
Thickness of the core layer	d_{F1}	15	nm
	d_{F2}	70	nm
Height of the channel ridge	h_1	2	nm
	h_2	0.7	nm
Thickness of SiO_2 subs. layer	d_S	1.25	μm
Thickness of SiO_2 cover layer	d_C	1.5	μm
Channel width	W	4	μm
Radius of 90°-bend	R_{bend}	10	mm
Radius of S-bend	$R_{S\text{-}bend}$	50	mm
Length of sensing windows	l	4	mm
Width of sensing windows	w_{win}	100	μm
Windows interdistance	l_{int}	3	mm
Distance between channels	d_{12}	60	μm
	d_{23}	80	μm
	d_{34}	100	μm

See text and Fig. 10.7 for a detailed description of each parameter
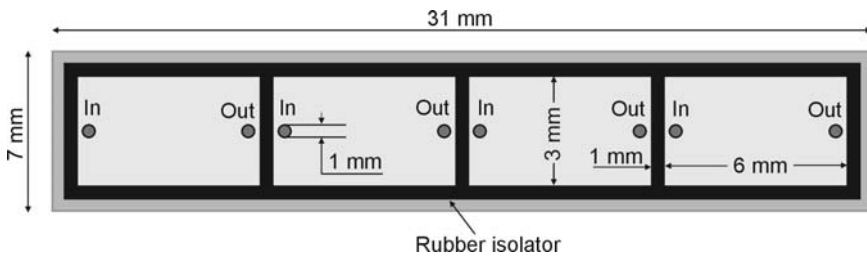

Fig. 10.8 *Bottom-view* of the four-chamber flow-through cuvette; each chamber has an In(let) and an Out(let), through which the sampling liquid flows to/from the sensing window. Reprinted from Ref. 31 with permission. © 2008 Optical Society of America

MS-REGLO; Ismatec SA., Glattbrugg, Switzerland) that has four separate pumping channels, each of them functioning independently from each other. In Fig. 10.9 a photograph of a flow-through cuvette assembled on the YI chip is shown.

The hybrid integration of the IO chip with a microfluidic system is treated in detail in Sect. 10.5.

10.3.3 Experimental Setup

Monochromatic laser light of an Ar^+ laser (Innova 70 Spectrum; Coherent, Inc., Santa Clara, CA) with a wavelength of 647 nm is end-fire coupled into the input fiber connected to the YI chip. The four output divergent beams overlap one another on the front side of a CCD camera (Teli CS-3440; 756 × 575 pixels, $w_{pixel} = 11.6$
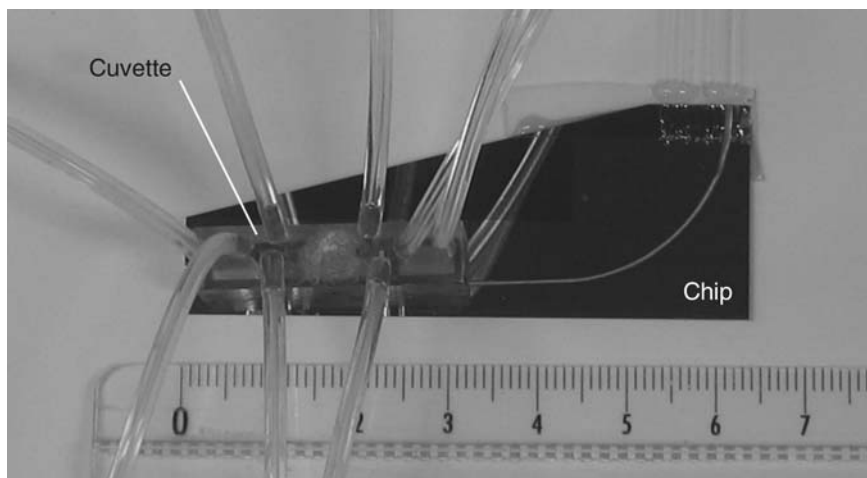
Fig. 10.9 Photograph of the sensor chip and the flow-through cuvette. The chip contains 11 four-channel YI sensors. The light is coupled into the chip by means of an optical fiber at the top-right-hand side. The light is transported to the sensing area by means of a curved channel waveguide, visible as a *white curved line*. Ruler indicates the dimensions in centimeters. Reprinted from Ref. 28 with permission. © 2008 American Chemical Society

μm; Tokyo Electronic Industry Co., Ltd., Tokyo, Japan) placed at a distance of ~60 mm from the chip endface and parallel to the endface plane for recording the interference pattern. The distance between the CCD camera and chip endface is chosen such that the recording area of the CCD camera can cover the total sum interference pattern, making use of all available pixels. A cylindrical lens is positioned between the chip endface and the CCD array for collimating the output divergent beams in the direction perpendicular to the sensor chip upper surface to collect all light emitted from the output channels. The recorded sum interference pattern is digitized to 12-bit information and analyzed by custom-written software in which a two-dimensional FFT algorithm is implemented. The algorithm recognizes and selects six different peaks that correspond to the six pairs of channels in the amplitude spectrum of the fast-Fourier-transformed interference pattern. The phase value corresponding to each pair of channels is extracted in the phase spectrum of the FFT at the given spatial frequencies. The maximum bandwidth of the measurement is 25 Hz, which is limited by the frame rate of the CCD camera.

10.3.4   Characterization

The performance of the realized YI sensor was first tested by applying solutions of different concentrations of glucose in water, thus inducing well-defined refractive index changes between measuring and reference channels of the device. In
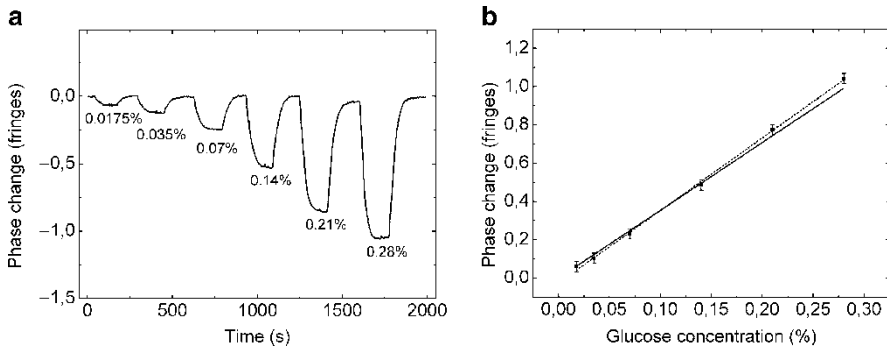
a

b

Fig. 10.10 (**a**) Response of the two-channel YI sensor to refractive index changes caused by applying six different glucose concentrations of 0.0175%, 0.035%, 0.07%, 0.14%, 0.21%, and 0.28% (by weight) intermitted by pure water to the measuring channel of the device. (**b**) Phase change vs. the glucose concentration: calculated (*line*), measured (*filled square*)), linear fit (*dotted line*)

Fig. 10.10a, the response of the sensor to different glucose concentrations applied in the sensing window of the measuring arm is shown. First pure water was flowed simultaneously over both sensing windows, and after several minutes, the flow in the measuring window was changed from water to 0.0175% (by weight) solution of glucose in pure water. When the signal stabilized, water was introduced and flowed over the measuring window. This procedure was repeated for five other glucose concentrations, respectively, 0.035%, 0.07%, 0.14%, 0.21%, and 0.28% (by weight). The induced refractive index changes, which can be calculated from the literature[36], vary from $\sim 2.4 \times 10^{-5}$ to $\sim 3.8 \times 10^{-4}$, whereas the corresponding phase changes vary from $\sim 0.062 \times 2\pi$ to $\sim 0.991 \times 2\pi$.

In Fig. 10.10b, the measured and expected phase changes as a function of the glucose concentration are plotted, including a linear fit of the measured data. The experimental plot (slope $\sim 3.8 \times 10^{-2} \times 2\pi$ ml/g) is in good accordance with the expected values (slope $\sim 3.5 \times 10^{-2} \times 2\pi$ ml/g).

The multichannel character of the YI sensor was tested by applying different glucose solutions to the different channels. In Fig. 10.11a, the response of the sensor is shown when a phase change of 2π was introduced in channel 1 and 3 and a phase change of $2 \times 2\pi$ was introduced in channel 2 simultaneously, using 0.616% and 1.232% (by weight) glucose solutions. Pure water was continuously flowed in channel 4. After a stable signal was reached, the solutions were exchanged for pure water, at first in channel 2, and next in channels 3 and 1, as shown in Fig. 10.11a. From the measured values, $\Delta\varphi_{12}$, $\Delta\varphi_{23}$, and $\Delta\varphi_{14}$, the phase change introduced in the channels, $\Delta\phi_1$, $\Delta\phi_2$, and $\Delta\phi_3$ can be determined, e.g., $\Delta\phi_1 = \Delta\varphi_{14} + \Delta\phi_4$, etc. Note that $\Delta\phi_4 = 0$, because no phase change was introduced in channel 4. The time-dependence of the phase changes are shown in Fig. 10.11b.

The obtained phase changes correspond well to the introduced changes, demonstrating one of the multipurpose features of the multichannel device with which
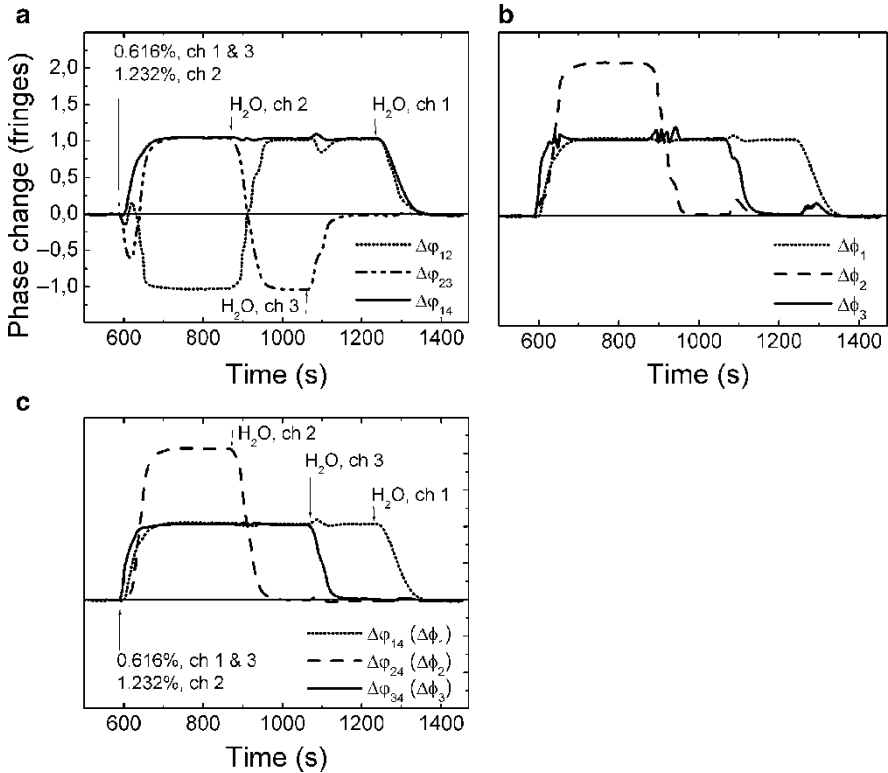
Fig. 10.11 (**a**) Measured phase changes $\Delta\varphi_{12}$, $\Delta\varphi_{23}$, and $\Delta\varphi_{14}$ as a function of time in the four-channel YI when a phase change of 2π was introduced in channel 1 and 3 and a phase change of $2 \times 2\pi$ in channel 2 simultaneously. (**b**) Phase changes that occur in channel 1, 2, and 3 ($\Delta\phi_1$, $\Delta\phi_2$, and $\Delta\phi_3$), calculated from measured phase changes $\Delta\varphi_{12}$, $\Delta\varphi_{23}$, and $\Delta\varphi_{14}$. (**c**) Measured phase changes $\Delta\varphi_{14}$, $\Delta\varphi_{24}$, and $\Delta\varphi_{34}$, which correspond to phase changes occurring in channel 1, 2, and 3, respectively. Reprinted from Ref. 31 with permission. © 2008 Optical Society of America

three different glucose concentrations were measured simultaneously and independently of each other. Alternatively, these channel phase changes can also be determined by using the measured phase changes $\Delta\varphi_{14}$, $\Delta\varphi_{24}$, and $\Delta\varphi_{34}$, as shown in Fig. 10.11c. Results obtained by both approaches correspond well, highlighting the consistency of the realized device. Fluctuations in the phase signal observed in Fig. 10.11b, c are caused by cross-talk[31] that is present when phase changes introduced in the channels are different from an integer number of fringes.

Figure 10.12 shows the phase difference measured between channels of each pair when no phase change was introduced in any of the channels. The phase resolution ($S/N = 1$) for each pair of channels, as determined from these measurements, is $\sim 1 \times 10^{-4} \times 2\pi$, which corresponds to a refractive index resolution of $\sim 8.5 \times 10^{-8}$ RIU (refractive index units) at a bandwidth of 1 Hz.
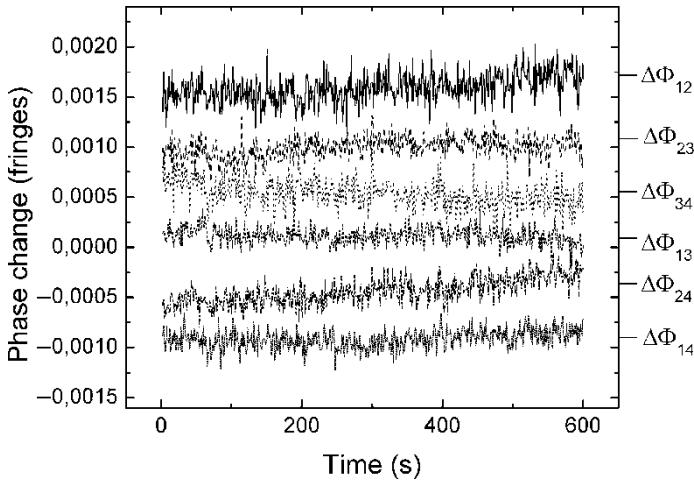
Fig. 10.12 Phase changes measured between two channels of each channel pair in the four-channel YI when no phase change was introduced at the channels. A shift of phase plots along vertical axis is applied to distinguish them from each other

10.4   Results

10.4.1   *Immunosensing Using the YI Sensor*

In an immunosensor the core-cover interface of an optical waveguide structure is coated with a chemo-optical transducer receptor layer, which can selectively bind to specific analyte molecules present in the cover medium. The receptor-analyte reaction obeys the law of mass action, which states that the rate of a reaction is proportional to the concentration of the reactants. At equilibrium, the rate of formation of the receptor-analyte complex is equal to the rate of breaking, and the equilibrium constant, K, can be written as

$$K = k_f/k_b = [\text{Re An}]/[\text{Re}] \cdot [\text{An}], \qquad (10.11)$$

where k_f and k_b are the formation and breaking rate constants and [Re], [An], and [ReAn] are, respectively, the concentration of receptor, analyte, and receptor-analyte complex. The thickness of the layer grown on the sensor surface due to the binding of analyte molecules to the receptor, Δw, depends on the receptor density, Γ_0, and the volume of the analyte molecules, V, and can be written as

$$\Delta w \approx \Delta F \Gamma_0 V, \qquad (10.12)$$

where ΔF is the fraction of receptor molecules that have bound an analyte molecule. The maximum fraction of receptor molecules bound to an analyte molecule as a function of concentration of the analyte molecules can be described by the Langmuir isotherm[43]

$$\Delta F_{\max} = \frac{K[\text{An}]}{1 + K[\text{An}]},$$ (10.13)

where K is the equilibrium constant for binding of the analyte molecules to the receptor molecules. In an interferometric sensor, such as the YI, the thickness of the protein layer grown on the sensor surface can be calculated as:

$$\Delta w = \frac{\lambda}{2\pi l}\left(\frac{\partial N_{\text{eff}}}{\partial w}\right)^{-1}\Delta\varphi.$$ (10.14)

Equations (10.14) and (10.8) can be used for estimation of the thickness and mass coverage of the receptor adsorbed to the sensor surface and of the analyte layer bound to the receptor layer.

The ratio between the number of bound analytes, N_{An}, and the number of receptors adsorbed, N_{Re}, can be derived as

$$\frac{N_{\text{An}}}{N_{Re}} \approx \frac{M_{Re}}{M_{\text{An}}} \cdot \frac{\Delta\varphi_{\text{An}}}{\Delta\varphi_{Re}},$$ (10.15)

where M_{An} and M_{Re} are the molecular weight of analyte and receptor, respectively, and $\Delta\varphi_{\text{An}}$ and $\Delta\varphi_{\text{Re}}$ are the phase changes that result from binding of analyte and receptor, respectively. Evaluation of this quantity yields information on the quality of the adhered receptor layer, e.g., maximum $N_{\text{An}}/N_{\text{Re}} = 2$ (receptor can bind maximum two analytes).

10.4.2   Materials

The protein A (pA), antihuman serum albumin (α-HSA, $M \sim 150$ kD), and human serum albumin (HSA, $M \sim 65$ kD) were provided by Paradocs BV (Tiel, The Netherlands). The Herpes Simplex Virus type 1 (HSV-1) and anti-HSV-1 gG glycoprotein G monoclonal antibody (α-HSV-1 gG) were purchased from Virusys Corporation (Marriottsville, MD, USA). Bovine serum albumin (BSA, $M \sim 50$ kD) was purchased from Sigma-Aldrich Chemie BV (Zwijndrecht, The Netherlands). Synthetic surface protein of Hepatitis-B virus generated in Hep-G2 cell-line (HEP G2, $M \sim 25$ kD) was provided by BioMerieux BV (Boxtel, The Netherlands). Phosphate buffered saline (PBS) was used for all experiments.

10.4.3   Protein Detection

In this section, use of the IO YI as an immunosensor is demonstrated, being relevant, e.g., for identification of biomarkers for early disease detection. The sensor is used to monitor the anti-human serum albumin - human serum albumin (α-HSA-HSA) immunoreaction.
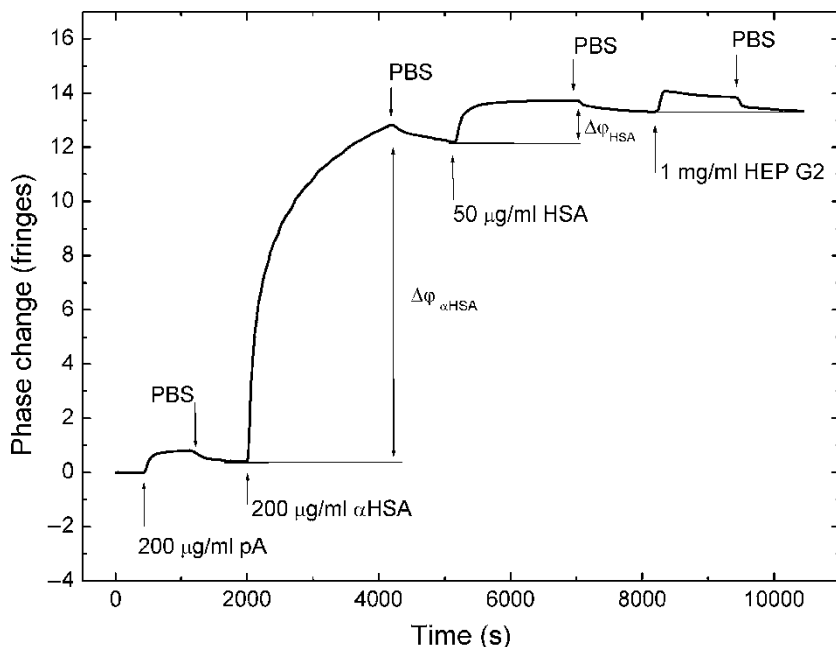
Fig. 10.13 Time-response between channels 1 and 4 in the four-channel YI sensor when the α-HSA-HSA immunoreaction was taking place in channel 1 and PBS buffer solution was continuously flowed in channel 4

Figure 10.13 shows the phase change measured between channels 1 and 4 of the four-channel YI when the PBS buffer solution has been continuously flowed in channels 2, 3, and 4, while in channel 1 the following steps were applied: first, a PBS buffer solution was flowed for ∼10 min. Then the flow was changed to a solution of protein A (pA) prepared in PBS with a concentration of 200 μg/ml. A pA-modified sensing surface is implemented in order to promote the binding and to ensure proper orientation of antibodies for further antigen binding[45,46]. After an equilibrium in the signal was achieved in ∼10 min, indicating the maximum amount of the pA adsorbed, the PBS buffer solution was flowed in channel 1 in order to get rid of the bulk refractive index effect. Physical adsorption of pA resulted in a phase change of ∼$0.5 \times 2\pi$, which is equivalent to a mass coverage of ∼0.12 mg/m^2, see (10.8).

Next, when a stable base line was achieved in ∼13 min, a concentration of 200 μg/ml solution of α-HSA in PBS was flowed in channel 1 for ∼30 min, and the flow was changed back to PBS buffer solution to correct for the bulk effect of α-HSA. Binding of α-HSA resulted in a phase change of ∼$12 \times 2\pi$, which corresponds to a mass coverage of ∼3.1 mg/m^2. Next, after the buffer solution was flowed for ∼10 min until a stable signal was achieved, a solution of 50 μg/ml HSA prepared in PBS was applied. Finally, the flow in channel 1 was changed back to PBS solution and

the phase change due to antigen layer formation was extracted. Binding of HSA caused a phase change of $\sim 1.3 \times 2\pi$. The thickness of the bound HSA layer to α-HSA molecules is found to be ~ 0.6 nm, see (10.14), assuming that there is only specific binding and a homogeneous layer was formed. The average number of HSA antigen molecules bound per one α-HSA antibody molecule is low (~ 0.25), see (10.15), indicating that there may be still antibody molecules available for binding. A larger binding in that case can be achieved by increasing the concentration of HSA antigen solutions, until the saturation level is reached, meaning that nearly all the available binding sites in the α-HSA layer are occupied by antigens. If the low number of 0.25 is due to improper orientation of α-HSA molecules, then little can be done.

Specificity of the α-HSA-HSA immunoreaction was checked by flowing in channel 1 a high concentration (1 mg/ml) of HEP G2 antigen solution prepared in PBS. After the flow was changed back to buffer solution, no response was observed, indicating that nonspecific binding of HEP G2 is negligible. This clearly demonstrates the specificity of α-HSA-HSA interaction.

Another possibility of the four-channel YI sensor is to measure different concentrations of a given analyte simultaneously. This feature was demonstrated experimentally by measuring simultaneously different concentrations of HSA, based on which the Langmuir binding curve (see (10.13)) was generated. For that purpose, three measuring channels, i.e., channel 1, 2, and 3, were simultaneously coated using a concentration of 200 µg/ml α-HSA prepared in PBS (PBS buffer solution was continuously flowed in channel 4). The next step consists of simultaneously applying three different concentrations of HSA, i.e., 500 ng/ml, 1 µg/ml, and 5 µg/ml in measuring channel 1, 2, and 3, respectively. This step was repeated by applying concentrations of 25 µg/ml, 50 µg/ml, and 100 µg/ml, in measuring channel 1, 2, and 3 simultaneously, followed by another set of concentrations (250 µg/ml, 500 µg/ml, and 1 mg/ml). After each set of concentrations was applied, PBS buffer solution was simultaneously flowed in the measuring channels to get rid of the bulk refractive index of HSA solutions applied. Finally, after coating channel 4 using 200 µg/ml α-HSA solution, concentrations of 100 ng/ml and 250 ng/ml HSA were applied successively (PBS was flowed in all other channels). The phase changes measured for the different HSA concentrations are plotted in Fig. 10.14.

The experimentally measured data are fitted with the Langmuir isotherm[43]. According to these measurements, when the concentration of HSA approaches ~ 1 mg/ml (1.5×10^{-5} M), a saturation level is reached, meaning that the antigen molecules already occupy all available binding sites. The total phase change measured due to HSA binding was $\sim 1.13 \times 2\pi$, corresponding to a layer thickness of ~ 0.5 nm. The equilibrium constant is estimated to be $\sim 3 \times 10^7$ M^{-1}, as extracted from a fitted Langmuir curve shown in Fig. 10.14, and is consistent with previous results[24].

From these results it is concluded that a pA-modified sensing surface is efficiently used to immobilize antibodies at the Si_3N_4 surface with a surface coverage of ~ 3 mg/m^2 corresponding to values found in literature[45,46]. However, the ratio
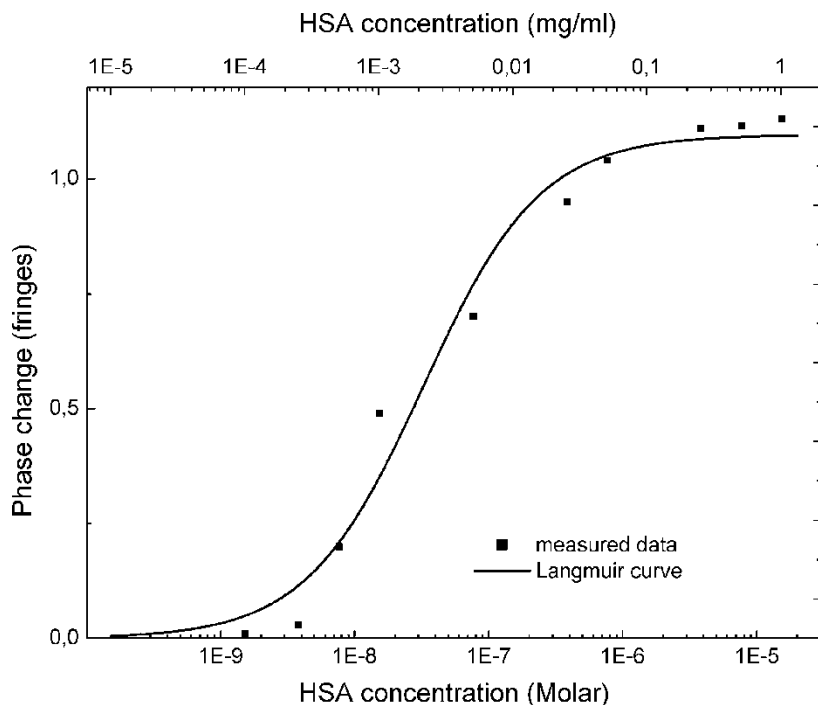
Fig. 10.14 Phase change measured in the four-channel YI for different concentrations of HSA solution. *Solid line* represents the Langmuir curve fitted to the experimental data

between the number of bound antigens and the number of antibodies (∼0.25) was lower than expected since theoretically two antigens can bind to one antibody. It should be note, however, that the used antigen concentrations were below the saturation value. The use of higher concentrations of HSA yielded slightly better results (ratio ∼0.3) indicating that there is still room for improvement. In addition, physical adsorption was used for immobilization of antibodies as an alternative to a pA-modified surface. In that case, postcoating with BSA after antibody adsorption was applied to prevent nonspecific binding of antigen. The results achieved with this method were less effective concerning the antibody immobilization (∼1.6 mg/m^2) and specificity. In addition, a signal drift after BSA adsorption was observed, which most likely is due to desorption of BSA from the surface.

In general, it is observed that after the binding step of proteins to the interface a gradual change of the phase is present (see, e.g., Fig. 10.13 after the α-HSA adsorption step). This effect can be explained by desorption of bound molecules not firmly attached. Given the time span used in these experiments, desorption did not seriously hamper the detection of analytes.

10.4.4 Virus Detection

One of the major challenges in the field of biosensors is the ability to detect and identify viruses. Viral outbreaks are a continuous threat to human populations and economies. Examples of recent viral outbreaks are H5N1 avian influenza and SARS. The extent of a viral outbreak depends, among other things, on currently available diagnostic capabilities. Existing methods like polymerase chain reaction (PCR)[47], branched-chain DNA (bDNA) tests[48], and enzyme-linked immunosorbent assay (ELISA)[49] are very sensitive, but have some major drawbacks. These techniques are very labor-intensive and require time-consuming sample preparation procedures. Therefore these techniques may have limited use for rapid responses in case of serious viral outbreaks. This drawback has motivated the development of many alternative techniques that may overcome the limitations of the existing methods. Among these, label-free detection schemes such as Raman[50,51], rupture event scanning[52], nanowires[53], microring resonators[10], and cantilever based techniques[54,55] are among the most promising. The YI sensor described here also is a good candidate for rapid viral detection.

The possibility to use the YI sensor for virus detection was explored by monitoring the interaction between α-HSV-1 gG antibody and HSV-1 virus particles. To this end, channel 1 was coated with protein pA as described in Sect. 10.4.2 followed by the immobilization of a α-HSV-1 gG layer on the sensing surface of channel 1. Channel 4 was used as a reference channel. Finally a solution with HSV-1 virus particles at a concentration of 10^5 particles/ml was added to channel 1. Figure 10.2 shows the phase change measured between channel 1 and reference channel 4, clearly demonstrating the detection of virus particles by the YI sensor (Fig. 10.15).

As a next step, the dynamic range and the sensitivity of the sensor was explored. Solutions with varying viral concentrations, ranging from 8.5×10^2 to 8.5×10^6 particles/ml were analyzed by measuring the corresponding phase changes when applied to the measuring channel of the sensor. The concentration range used corresponds to the classification "very low" to "very high" in terms of the viral load[56]. The result of this experiment is shown in Fig. 10.16a and demonstrates that a large dynamic range of at least 4 orders of magnitude is achieved, covering the entire clinically relevant concentration range.

Finally, the specificity of the virus sensor was addressed by detecting virus particles suspended in complex samples such as human blood serum. To do so, HSV-1 virus particles were spiked into human blood serum at a concentration of 10^5 particles/ml. The response of the sensor to the application of the HSV-1/serum sample is shown in Fig. 4.4b. Here we first added serum (with no virus particles present) to the measuring channel, which was followed by adding virus-containing serum. The results as shown in Fig. 4.4b, clearly demonstrates the feasibility to detect the binding of HSV-1 in the presence of serum. The observed phase change is in good agreement with the measurement of HSV-1 in buffer as indicated in Fig. 10.16a. To further confirm the specificity of HSV-1–α-HSV-1 gG interaction, a
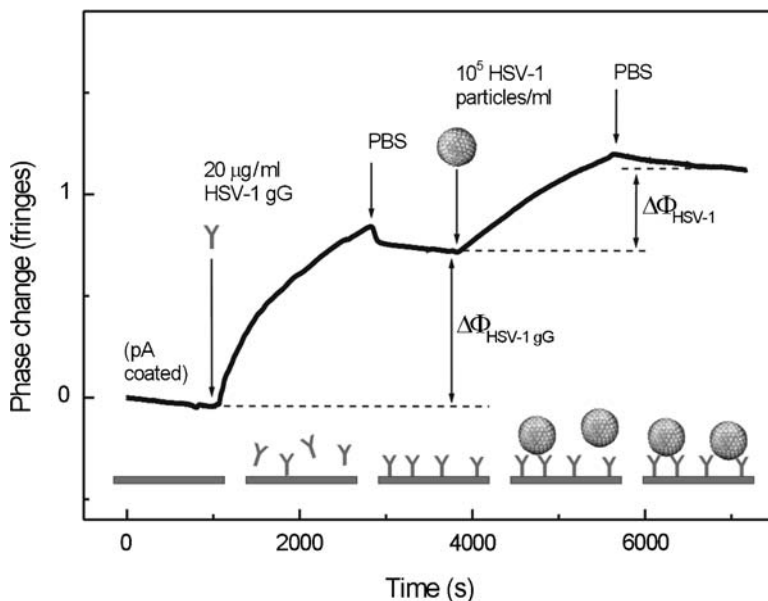
Fig. 10.15 Virus detection test. Sensor signal (phase change) measured between channel 1 and the reference channel for the immobilization of anti-HSV-1 glycoprotein G monoclonal antibody layer on the sensing surface of channel 1 ($\Delta\Phi_{\text{HSV-1 gG}}$) and the binding of HSV-1 particles to this layer ($\Delta\Phi_{\text{HSV-1}}$). Reprinted from Ref. 28 with permission. © 2008 American Chemical Society
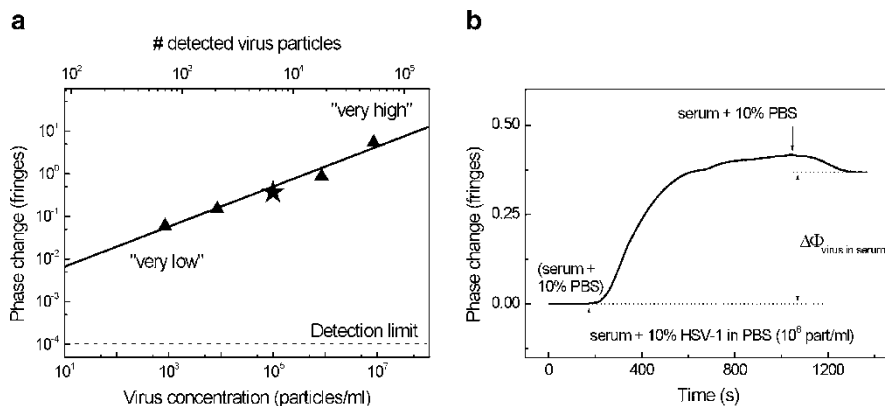

Fig. 10.16 Measurement of different HSV-1 concentrations and detection in serum. (**a**) Phase change measured for different concentrations of HSV-1 sample solutions in PBS applied in the measuring channel of the YI sensor (*filled triangle*). *Solid line* is a linear-fit of the experimental data, φ represents the phase change measured for HSV-1 diluted in serum (see Fig. 16b), *dashed line* indicates the phase detection limit of the sensor. (**b**) Sensor response due to the binding of HSV-1 diluted in serum. Final concentration of HSV-1 was 10^5 particles/ml. The total signal is estimated to be $\Delta\Phi_{\text{virus in serum}} = 0.37$ fringes, consistent with results obtained in PBS (see φ in Fig. 16a). Reprinted from Ref. 28 with permission. © 2008 American Chemical Society

control experiment in which no antibody was immobilized in the measuring channel was performed. No response was measured when the virus solution in serum was applied (graph not shown), indicating the specificity of HSV-1–α-HSV-1 gG interaction. These results show the possibility to specifically detect capture of HSV-1 particles, even at very low particle concentrations and at a low number of virus particles.

In the clinically relevant concentration range[56] the relation between the response of the sensor and the viral concentration is linear (a linear fit through the data points in Fig. 10.16a gives a correlation coefficient of 0.98) facilitating easy virus concentration predictions with a calibrated sensor. Furthermore, even at the lowest measured virus concentration (850 particles/ml) a high signal-to-noise ratio of 2×10^2 (at a bandwidth of 0.1 Hz) is achieved. Therefore it is predicted that the current YI sensor is able to detect even much lower concentrations. An estimation of the number of captured HSV-1 particles can be made given the size (150–200 nm)[57] and the refractive index ($\sim$1.41)[58]. This results in a phase change of $\sim$1.1 $\times$ 10^{-4} fringes for the binding of a single virus particle. From this estimation it is derived that for the lowest measured concentration $\sim$700 virus particles were detected with an average binding rate of 1 virus every 4 s. Given the detection limit of the sensor (10^{-4} fringes) it can be argued that the capture of a single virus particle at the sensor surface might yield a detectable signal.

The YI sensor also enables specific detection of virus particles in human blood serum. Even though there is a background signal caused by nonspecific binding of serum proteins, the signal due to binding of virus particles is readily detected. Although the background remains a drawback of this approach, alternative detection schemes with the YI sensor such as the use of differential phase change information from different measuring channels may be applied to reduce the influence of the background considerably. Moreover, attention should be paid to improvement of the measuring channel coatings, which should result in further reduction of the background.

10.4.5 Multianalyte Detection

Having demonstrated the possibility to use the IO YI as an immunosensor, in this section the multipurpose feature of the sensor is shown by monitoring more than one analyte simultaneously. These tests are performed by immobilizing different receptor layers in adjacent measuring channels and monitoring the sensor response to different analyte solutions. To do so, antihuman serum albumin (α-HSA; Sigma-Aldrich, St. Louis, MO, United States) was immobilized in channel 1 by flowing a 200 μg/ml α-HSA solution prepared in PBS. In channel 2, α-HSV-1 gG was immobilized. Next, a solution of 50 μg/ml human serum albumin (HSA; Sigma-Aldrich, St. Louis, MO, United States) in PBS was simultaneously applied in channels 1 and 2 and after approximately 30 min, flow was changed back to PBS for both channels. The observed binding curves are shown in Fig. 10.17 (graphs A1
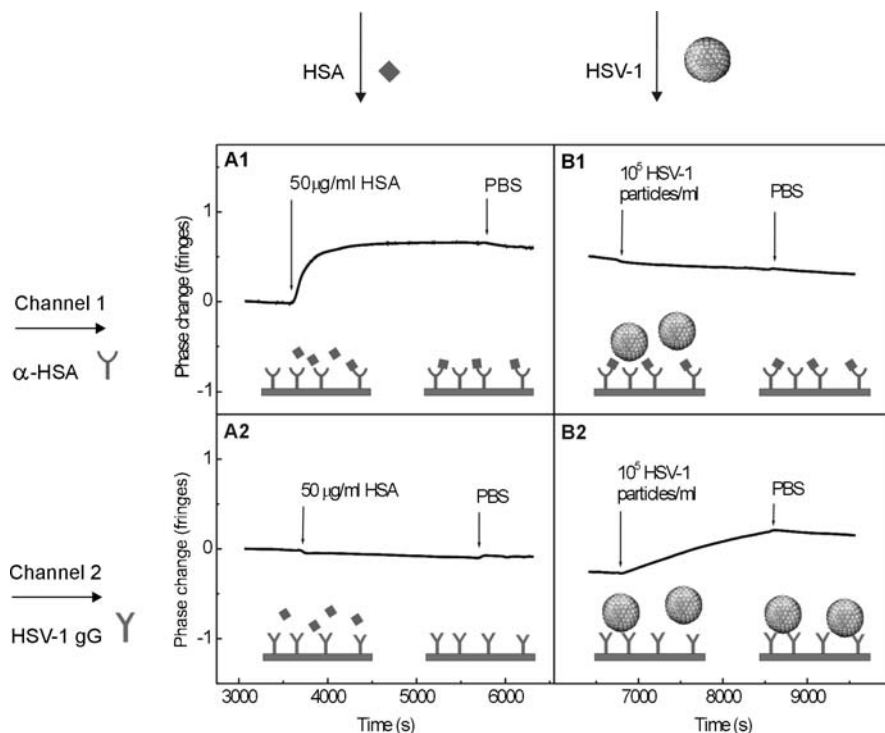
Fig. 10.17 Specific detection of HSV-1. Phase changes $\Delta\Phi14$ and $\Delta\Phi24$ in the four-channel YI sensor as a function of time during several processes. HSA solution was first flowed through channels 1 and 2 simultaneously (A1 and A2). Next, after washing with PBS, HSV-1 solution was flowed in channels 1 and 2 simultaneously (B1 and B2); PBS was continuously flowed in reference channel 4. Thus, the four graphs show the following interactions: (A1) α-HSA-HSA, (A2) α-HSV-1 gG-HSA, (B1) α-HSA-HSV-1, (B2) α-HSV-1 gG-HSV-1. Note that initial phases in A1 and A2 were shifted to 0 for clarity. Reprinted from Ref. 28 with permission. © 2008 American Chemical Society

and A2, respectively). After achievement of a stable baseline, a 10^5 particles/ml HSV-1 solution was flowed in both channels (see B1 and B2 in Fig. 10.17, respectively). The observation that a response is measured only for the α-HSA-HSA and α-HSV-1 gG-HSV-1 interactions is a clear indication that the signals are caused by specific interactions and that crossreactivity between coatings is negligible.

10.5   A Hybrid YI-Sensor Microfluidic Chip

The main advantages of the current YI sensor are that it is extremely sensitive, is a label-free technique, has multiplexing capabilities, and allows for a compact design. As such it is a good candidate for the development of a reliable handheld

device that can be used in the field to quickly and easily detect, e.g., viruses from either human or animal body fluid samples. To this end the integration of the chip with microfluidic sample handling would strongly enhance the robustness and compactness of the sensor.

Figure 10.18 shows a four-channel YI sensor chip integrated with a microfluidic system[42]. The microfluidic system was designed such that each measuring channel can be addressed individually. The channels are fabricated in a transparent glass plate with cross-sectional dimensions of 200 μm × 15 μm. The glass plate is glued onto the IO-chip using a UV curable resin. A major advantage of the microfluidic system over the cuvette system is, apart from the improved robustness of the sensor, the strongly enhanced time-response of the sensor. Experiments on monitoring the antihuman serum albumin/human serum albumin immunoreaction show that the response time of the sensor of 100 s achieved with a bulky cuvette, is reduced to 4 s (at similar sample flow). This improvement is due to the much smaller dimensions of the microfluidic channels compared to those of the cuvette. Reduced dimensions, especially the height of the flow channel, imply higher flow velocities at the sample-sensor surface interface and shorter diffusion times of molecules/analytes.
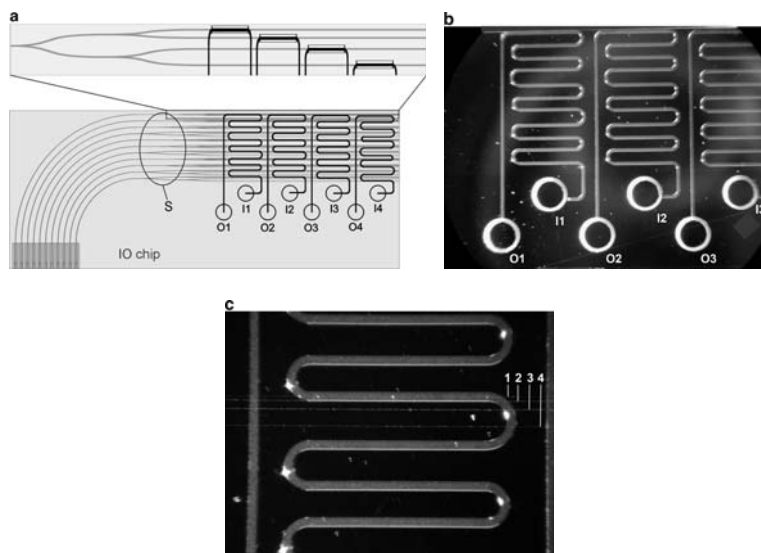

Fig. 10.18 Hybrid sensing platform obtained by bonding a glass microfluidic system to an IO four-channel YI chip. (**a**) *Top-view* of the microfluidic system. The optical chip contains configurations of YI sensor structure, which have different distances between their output channels, resulting in a different length of splitting function, manifested by different starting positions of the first Y-junction (see S in **a**). (**b**) *Close-view* micrograph of microfluidic channel 1, 2, and 3. (**c**) *Close-view* micrograph showing the light propagating through waveguide channel 1, 2, 3, and 4, and the microfluidic channel 2 addressing the sensing window of the waveguide channel 2. Ii and Oi indicate the input and output, respectively, of microfluidic channel *i*, addressing the *i*th bundle of sensing windows. Dimensions of the microfluidic sensing system are 63 mm × 24 mm. (**a**) is reprinted from Ref. 42 with permission. © 2008 Elsevier. (**b**) and (**c**) are reprinted from Ref. 59 with permission. © 2008 Expert Reviews Ltd

Both aspects improve the time-response of the sensor. In addition the total sample volume required is also strongly reduced from the sub-ml to the µl range.

10.6   Discussion and Conclusions

As demonstrated, the YI sensor can be used to detect analytes such as proteins and viruses with a very high sensitivity. The sensitivity obtained with, the 4-channel YI sensor is ~20 fg/mm^2 with, ~2 orders of magnitude higher than other label-free sensor techniques such as the well established SPR sensor[60]. Additional experiments with a two-channel YI sensor with longer interaction lengths (20 mm rather that 4 mm) show an even higher sensitivity of ~1 fg/mm^2 [41]. Moreover, the YI sensor is simple, easy to use, and compact, providing excellent possibilities for development of portable point-of-care devices. The detectable concentrations of analytes in a sample approach those required in clinical diagnostics assays, which could be an attractive market for these types of sensors. This is further motivated by the ability to integrate the sensor with efficient microfluidic-based fluid delivery systems[42], resulting in a much faster time response of the sensor. In addition, the sensor manufacturing technology is suitable for mass production, allowing important scale-based costs reduction.

The high sensitivity of the sensor that is demonstrated is obviously very promising. However, to be suitable for application in the field of clinical diagnostics assays the sensor also has to specific. The sensor signal should only be sensitive to the binding of the analyte of interest and not to other molecules or viruses in the sample. Therefore it is extremely important that these types of sensors are tested with clinically relevant samples. Specificity of the sensor thus strongly depends on the "chemical" coating of the sensor surface. The use of a pA-based coating was used to successfully detect HSV-1 viruses in human blood serum (this work) at clinically relevant concentrations. More recently it was shown that tuberculosis-specific antibodies can be detected with a YI sensor in undiluted human blood serum[39]. The availability of antibodies with high-specificity and low crossreactivity for relevant antigens, combined with these results suggest that YI-based sensors can combine very high sensitivity with good specificity and therefore provide a solid foundation for further development of YI sensors for clinical diagnostic assays.

References

 1 Hong, J. G.; Choi, J. S.; Han, G. Y.; Kang, J. K.; Kim, C. M.; Kim, T. S.; Yoon, D. S., A Mach-Zehnder interferometer based on silicon oxides for biosensor applications, *Anal. Chim. Acta* **2006**, 573, 97–103

 2 Heideman, R. G.; Kooyman, R. P. H.; Greve, J., Performance of a highly sensitive optical wave-guide Mach-Zehnder interferometer immunosensor, *Sens. Actuators B-Chem.* **1993**, 10, 209–217

3 Schipper, E. F.; Brugman, A. M.; Dominguez, C.; Lechuga, L. M.; Kooyman, R. P. H.; Greve, J., The realization of an integrated Mach-Zehnder waveguide immunosensor in silicon technology, *Sens. Actuators B-Chem.* **1997**, 40, 147–1534.

4 Duport, I. S.; Benech, P.; Rimet, R., New integrated-optics interferometer in planar technology, *Appl. Opt.* **1994**, 33, 5954–5958

5 Stamm, C.; Lukosz, W., Integrated optical difference interferometer as immunosensor, *Sens. Actuators B-Chem.* **1996**, 31, 203–207

6 Cox, E. R.; Jones, B. E. Fiber optic color sensors based on Fabry-Perot interferometry, In First International Conference on Optical Fiber Sensors, London, 1993

7 Clerc, D.; Lukosz, W., Integrated optical output grating coupler as biochemical sensor, *Sens. Actuators B-Chem.* **1994**, 19, 581–586

8 Cush, R.; Cronin, J. M.; Stewart, W. J.; Maule, C. H.; Molloy, J.; Goddard, N. J., The resonant mirror - a novel optical biosensor for direct sensing of biomolecular interactions. 1. Principle of operation and associated instrumentation, *Biosens. Bioelectron.* **1993**, 8, 347–353

9 Krioukov, E.; Klunder, D. J. W.; Driessen, A.; Greve, J.; Otto, C., Sensor based on an integrated optical microcavity, *Opt. Lett.* **2002**, 27, 512–514

10 Zhu, H. Y.; White, I. M.; Suter, J. D.; Zourob, M.; Fan, X. D., Opto-fluidic micro-ring resonator for sensitive label-free viral detection, *Analyst* **2008**, 133, 356–360

11 Armani, A. M.; Kulkarni, R. P.; Fraser, S. E.; Flagan, R. C.; Vahala, K. J., Label-free, single-molecule detection with optical microcavities, *Science* **2007**, 317, 783–787

12 Sun, Y. Z.; Shopova, S. I.; Frye-Mason, G.; Fan, X. D., Rapid chemical-vapor sensing using optofluidic ring resonators, *Opt. Lett.* **2008**, 33, 788–790

13 Kooyman, R. P. H.; Lenferink, A. T. M.; Eenink, R. G.; Greve, J., Vibrating mirror surface-plasmon resonance immunosensor, *Anal. Chem.* **1991**, 63, 83–85

14 Densmore, A.; Xu, D. X.; Janz, S.; Waldron, P.; Mischki, T.; Lopinski, G.; Delage, A.; Lapointe, J.; Cheben, P.; Lamontagne, B.; Schmid, J. H., Spiral-path high-sensitivity silicon photonic wire molecular sensor with temperature-independent response, *Opt. Lett.* **2008**, 33, 596–598

15 Brecht, A.; Piehler, J.; Lang, G.; Gauglitz, G., A direct optical immunosensor for atrazine detection, *Anal. Chim. Acta* **1995**, 311, 289–299

16 Lambeck, P. V., Integrated opto-chemical sensors, *Sens. Actuators B-Chem.* **1992**, 8, 103–116

17 Heideman, R. G.; Lambeck, P. V., Remote opto-chemical sensing with extreme sensitivity: design, fabrication and performance of a pigtailed integrated optical phase-modulated Mach-Zehnder interferometer system, *Sens. Actuators B-Chem.* **1999**, 61, 100–127

18 Brandenburg, A., Differential refractometry by an integrated-optical Young interferometer, *Sens. Actuators B-Chem.* **1997**, 39, 266–271

19 Brandenburg, A.; Krauter, R.; Kunzel, C.; Stefan, M.; Schulte, H., Interferometric sensor for detection of surface-bound bioreactions, *Appl. Opt.* **2000**, 39, 6396–6405

20 Cross, G. H.; Ren, Y. T.; Freeman, N. J., Young's fringes from vertically integrated slab waveguides: Applications to humidity sensing, *J. Appl. Phys.* **1999**, 86, 6483–6488

21 Cross, G. H.; Reeves, A. A.; Brand, S.; Popplewell, J. F.; Peel, L. L.; Swann, M. J.; Freeman, N. J., A new quantitative optical biosensor for protein characterisation, *Biosens. Bioelectron.* **2003**, 19, 383–390

22 Koster, T.; Lambeck, P., Fully integrated optical polarimeter, *Sens. Actuators B-Chem.* **2002**, 82, 213–226

23 Heideman, R. G. Optical Wabeguide Based Evanescent Field Immunosensors, University of Twente, Enschede, The Netherlands, 1993

24 Heideman, R. G.; Kooyman, R. P. H.; Greve, J., Immunoreactivity of adsorbed antihuman chorionic-gonadotropin studied with an optical wave-guide interferometric sensor, *Biosens. Bioelectron.* **1994**, 9, 33–43

25 Schipper, E. F.; Bergevoet, A. J. H.; Kooyman, R. P. H.; Greve, J., New detection method for atrazine pesticides with the optical waveguide Mach-Zehnder immunosensor, *Anal. Chim. Acta* **1997**, 341, 171–176

26 Schipper, E. F. Waveguide Immunosensing of Small Molecules, University of Twente, Enschede, The Netherlands, 1997

27 Minson, A. C., Alphaherpesviruses: herpes simplex and varicella zoster virus infection, In Topley and Wilson's Microbiology And Microbial Infections, 9th edn.; Mahy, B.; Collier, L., Eds.; Arnold, London, 1998, Vol. 1, 325–339

28 Ymeti, A.; Greve, J.; Lambeck, P. V.; Wink, T.; van Hovell, S.; Beumer, T. A. M.; Wijn, R. R.; Heideman, R. G.; Subramaniam, V.; Kanger, J. S., Fast, ultrasensitive virus detection using a young interferometer sensor, *Nano Lett.* **2007**, 7, 394–397

29 Xu, J.; Suarez, D.; Gottfried, D. S., Detection of avian influenza virus using an interferometric biosensor, *Anal. Bioanal. Chem.* **2007**, 389, 1193–1199

30 Wilson, J.; Hawkes, J. F. B., *Optoelectronics, An Introduction*. Prentice Hall, London, 1989

31 Ymeti, A.; Kanger, J. S.; Greve, J.; Lambeck, P. V.; Wijn, R.; Heideman, R. G., Realization of a multichannel integrated Young interferometer chemical sensor, *Appl. Opt.* **2003**, 42, 5649–5660

32 Hecht, E., *Optics*, Addison Wesley, Reading, MA, 1998

33 Ymeti, A.; Kanger, J. S.; Wijn, R.; Lambeck, P. V.; Greve, J., Development of a multichannel integrated interferometer immunosensor, *Sens. Actuators B-Chem.* **2002**, 83, 1–7

34 Defeijter, J. A.; Benjamins, J.; Veer, F. A., Ellipsometry as a tool to study adsorption behavior of synthetic and biopolymers at air-water-interface, *Biopolymers* **1978**, 17, 1759–1772

35 Weast, R. C., Handbook of Chemistry and Physics, 65th edn.; CRC Press, Boca Raton, FL, 1984

36 Parriaux, O.; Veldhuis, G. J., Normalized analysis for the sensitivity optimization of integrated optical evanescent-wave sensors, *J. Lightwave Technol.* **1998**, 16, 573–582

37 Haruna, M.; Segawa, Y.; Nishihara, H., Nondestructive and simple method of optical-waveguide loss measurement with optimization of end-fire coupling, *Electron. Lett.* **1992**, 28, 1612–1613

38 Nagel, T.; Ehrentreich-Forster, E.; Singh, M.; Schmitt, K.; Brandenburg, A.; Berka, A.; Bier, F. F., Direct detection of tuberculosis infection in blood serum using three optical label-free approaches, *Sens. Actuators B-Chem.* **2008**, 129, 934–940

39 Parishi, G. I.; Haszko, S. E.; Rozgonyi, G. A., Tapered windows in SiO_2:the effect of $NH4F$:HF dilution and etching temperature, *J. Electrochem. Soc. Solid State Sci. Technol.* **1997**, 124, 917–921

40 Ymeti, A. Development of a Multichannel Integrated Young Interferometer Immunosensor, University of Twente, Enschede, The Netherlands, 2004

41 Ymeti, A.; Kanger, J. S.; Greve, J.; Besselink, G. A. J.; Lambeck, P. V.; Wijn, R.; Heideman, R. G., Integration of microfluidics with a four-channel integrated optical Young interferometer immunosensor, *Biosens. Bioelectron.* **2005**, 20, 1417–1421

42 Antrade, J. D., Principles of protein adsorption, In Surface and Interfacial Aspects of Biomedical Polymers; Antrade, J. D., Ed.; Plenum Press, New York, 1985, Vol. 2

43 Owaku, K.; Goto, M.; Ikariyama, Y.; Aizawa, M., Optical immunosensing for IgG, *Sens. Actuators B-Chem.* **1993**, 14, 723–724

44 Lu, B.; Smyth, M. R.; Okennedy, R., Oriented immobilization of antibodies and its applications in immunoassays and immunosensors, *Analyst* **1996**, 121, R29–R32

45 Piatak, M.; Saag, M. S.; Yang, L. C.; Clark, S. J.; Kappes, J. C.; Luk, K. C.; Hahn, B. H.; Shaw, G. M.; Lifson, J. D., High-levels of HIV-1 in plasma during all stages of infection determined by competitive PCR, *Science* **1993**, 259, 1749–1754

46 Pachl, C.; Todd, J. A.; Kern, D. G.; Sheridan, P. J.; Fong, S. J.; Stempien, M.; Hoo, B.; Besemer, D.; Yeghiazarian, T.; Irvine, B.; Kolberg, J.; Kokka, R.; Neuwald, P.; Urdea, M. S., Rapid and precise quantification of HIV-1 RNA in plasma using a branched DNA signal amplification assay, *J. Acquir. Immune Defic. Syndr. Hum. Retrovirol.* **1995**, 8, 446–454

47 Kumarasamy, V.; Wahab, A. H. A.; Chua, S. K.; Hassan, Z.; Chem, Y. K.; Mohamad, M.; Chua, K. B., Evaluation of a commercial dengue NS1 antigen-capture ELISA for laboratory diagnosis of acute dengue virus infection, *J. Virolog. Methods* **2007**, 140, 75–79

48 Shanmukh, S.; Jones, L.; Driskell, J.; Zhao, Y. P.; Dluhy, R.; Tripp, R. A., Rapid and sensitive detection of respiratory virus molecular signatures using a silver nanorod array SERS substrate, *Nano Lett*. **2006**, 6, 2630–2636

49 Shanmukh, S.; Jones, L.; Zhao, Y. P.; Driskell, J. D.; Tripp, R. A.; Dluhy, R. A., Identification and classification of respiratory syncytial virus (RSV) strains by surface-enhanced Raman spectroscopy and multivariate statistical techniques, *Anal. Bioanal. Chem*. **2008**, 390, 1551–1555

50 Cooper, M. A.; Dultsev, F. N.; Minson, T.; Ostanin, V. P.; Abell, C.; Klenerman, D., Direct and sensitive detection of a human virus by rupture event scanning, *Nat. Biotechnol*. **2001**, 19, 33–837

51 Patolsky, F.; Zheng, G. F.; Hayden, O.; Lakadamyali, M.; Zhuang, X. W.; Lieber, C. M., Electrical detection of single viruses, *Proc. Natl. Acad. Sci. USA* **2004**, 101, 14017–14022

52 Gupta, A.; Akin, D.; Bashir, R., Single virus particle mass detection using microresonators with nanoscale thickness, *Appl. Phys. Lett*. **2004**, 84, 1976–1978

53 Owen, T. W.; Al-Kaysi, R. O.; Bardeen, C. J.; Cheng, Q., Microgravimetric immunosensor for direct detection of aerosolized influenza A virus particles, *Sens. Actuators B-Chem*. **2007**, 126, 691–699

54 Mellors, J. W.; Rinaldo, C. R.; Gupta, P.; White, R. M.; Todd, J. A.; Kingsley, L. A., Prognosis in HIV-1 infection predicted by the quantity of virus in plasma, *Science* **1996**, 272, 1167–1170

55 Levine, A. J., Viruses, Scientific American Library, New York, 1992

56 Balch, W. M.; Vaughn, J.; Novotny, J.; Drapeau, D. T.; Vaillancourt, R.; Lapierre, J.; Ashe, A., Light scattering by viral suspensions, *Limnol. Oceanogr*. **2000**, 45, 492–498

57 Ymeti, A.; Subramaniam, V.; Beumer, T. A. M.; Kanger, J. S., An ultrasensitive Young interferometer handheld sensor for rapid virus detection, *Expert Rev. Med. Devices* **2007**, 4, 447–454

58 Berger, C. E. H.; Beumer, T. A. M.; Kooyman, R. P. H.; Greve, J., Surface plasmon resonance multisensing, *Anal. Chem*. **1998**, 70, 703–706